International Journal of Hydrogen Energy

Facile fabrication of CuScS2/CoO as an efficient electrocatalyst for oxygen evolution reaction and water treatment process

--Manuscript Draft--

Manuscript Number:	HE-D-23-04192R1
Article Type:	Full Length Article
Section/Category:	Electrolysis / Electrolyzers
Keywords:	CuScS2/CoO; Nanocomposite; Synergistic Effect; OER
Corresponding Author:	Sumaira Manzoor PAKISTAN
First Author:	Asma Alothman
Order of Authors:	Asma Alothman
	Karam Jabbour
	Sumaira Manzoor
	Abdul Ghafoor Abid
	Mehar Un Nisa
	Pablo Hernandez Gomez
	Saikh Wabaidur
	Mika Sillanpää
Abstract:	A major issue is the production of green and sustainable energy while the development of an effective, affordable, readily available with a higher rate of oxygen and hydrogen evolution reactions is need of the time. Here in present work, we fabricated CuScS2, CoO, and CuScS2/CoO to replace the extremely expensive Pt/C and IrO2 that are employed as the benchmark materials for water electrolysis. We have also investigated their electrochemical performance in an alkaline environment for the oxygen evolution reaction (OER). The CuScS2/CoO nanocomposite is more effective electrode material than CuScS2 and CoO. The composite material shows smaller overpotential (179 mV) and reduced Tafel slope (46 mV dec-1) value than individual materials to attain a current density of 10 mA cm-2. The better efficiency of the composite material is due to well-distinct good shape with greater BET surface area, and relatively small resistance to charge transfer. Furthermore, the CuScS2/CoO exhibits remarkable electrocatalytic as well as photocatalytic performance in comparison to CuScS2 and CoO. This research provides a valuable guide for developing an OER electrocatalyst in an alkaline medium and shows better electrochemical as well as photocatalytic performance of CuScS2/CoO nanomaterials.

Facile fabrication of $CuScS_2/CoO$ as an efficient electrocatalyst for oxygen evolution reaction and water treatment process

Asma A. Alothman[a], Karam Jabbour[b], Sumaira Manzoor[c,*], Abdul Ghafoor Abid[c], Mehar Un Nisa[c], Pablo Herndez Gomez[d], Saikh M. Wabaidur[a], Mika Sillanpää[e]

[a] Department of Chemistry, College of Science, King Saud University, Riyadh 11451, Saudi Arabia

[b] College of Engineering and Technology, American University of the Middle East, Egaila-54200, Kuwait

[c] Institute of Chemical Sciences, Bahauddin Zakariya University, Multan

[d] Departmento de Eletricidad y Electronica, Unversidad de Valladolid, Valladolid, Spain

[e] Department of Biological and Chemical Engineering, Aarhus University, Norrebrogade 44, 8000 Aarhus C, Denmark

*= Corresponding Author

E-mail: sumairamanzoor672@gmail.com

Abstract

A major issue is the production of green and sustainable energy while the development of an effective, affordable, readily available with a higher rate of oxygen and hydrogen evolution reactions is need of the time. Here in present work, we fabricated $CuScS_2$, CoO, and $CuScS_2/CoO$ to replace the extremely expensive Pt/C and IrO_2 that are employed as the benchmark materials for water electrolysis. We have also investigated their electrochemical performance in an alkaline environment for the oxygen evolution reaction (OER). The $CuScS_2/CoO$ nanocomposite is more effective electrode material than $CuScS_2$ and CoO. The composite material shows smaller overpotential (179 mV) and reduced Tafel slope (46 mV dec^{-1}) value than individual materials to attain a current density of 10 mA cm^{-2}. The better efficiency of the composite material is due to well-distinct good shape with greater BET surface area, and relatively small resistance to charge transfer. Furthermore, the $CuScS_2/CoO$ exhibits remarkable electrocatalytic as well as photocatalytic performance in comparison to $CuScS_2$ and CoO. This research provides a valuable guide for developing an OER electrocatalyst in an alkaline medium and shows better electrochemical as well as photocatalytic performance of $CuScS_2/CoO$ nanomaterials.

Keywords: $CuScS_2/CoO$; Nanocomposite; Synergistic effect; OER

1. Introduction

As human society and industrialization have advanced quickly over time, severe energy and environmental problems have emerged, forcing researchers to concentrate on sustainable and environmentally friendly energy resources to make up for the shortage of fossil fuel-based energy sources [1-3]. Because of their high ion transportation efficiency, ability to produce alternative energy sources, and other factors, the most promising alternative energy conversion and storage systems, such as Li-ion batteries, Zn-air batteries, water electrolysis and fuel cells have attracted much attention in this context recently [4-6]. Among all these procedures, water electrolysis results in the generation of hydrogen and oxygen, both of which are suppliers of pure, sustainable power [7, 8]. The OER, one of the two half-reactions that comprise the total water electrolysis, is more difficult because it involves a four-proton-coupled electron transport reaction mechanism and is extremely kinetically slow [9, 10]. Significant overpotential is also essential for this process, severely limiting its application in both commercial and industrial electrolytic energy systems [11, 12]. Even while precious metal-based catalysts like IrO_2, RuO_2, Pt/C, and Ir black are commonly recognized for commercial usage, there are several limitations to their utilization on a huge scale, including an absence of availability, poor stability and high price efficiency [13].

The development of efficient and reliable non-noble metal-based electrode materials for water electrolysis is therefore highly desirable. One of the effective earth-abundant electrocatalysts has been recognized as transition metal-based nanomaterials [14-16]. Metal oxides, metal-organic frameworks, metal sulphides, layered double hydroxides, transition metal-based phosphates/phosphonates/phosphides, metal chalcogenides, bimetallic oxides, and other types of electrode materials have all been developed for electrolytic oxygen evolution reactions [17, 18]. Metal oxides have received the most interest among these nanomaterials for electrolytic OER in alkaline medium because of their inexpensive cost, simple production process, and high stability [19, 20]. Because of their high thermal and structural durability, strong conductance, and notable uses in electrochemical energy conversion, storage, and catalysis, porous cobalt oxides have been synthesized in various strategic pathways [20-22]. Additionally, limited conductance reduces the availability of the cobalt oxides' catalyst surface, which limits the effectiveness of electrolytic OER [23, 24]. Thus, various tactical approaches have recently been used to enhance the OER performance of the electrode material, including doping with the other elements, conductive supports, incorporation of vacant positions, control of the metal facet sequence, and synergistic effects in nanostructured materials [25-27].

On the other hand, textile [28], plastic [29], pharmaceutical [30], printing [31], leather [32], cosmetics [33], food processing [34], and dye manufacturing sectors discharge wastewater loaded with synthetic colors that constitute a severe hazard to aquatic life and the ecology [35]. Because these dyes are stable and non-biodegradable, they must be removed from wastewater before it reaches the aquatic system [36]. Several techniques have been used to remove these colors from the effluent, such as adsorption, photocatalytic degradation, membrane filtering, coagulation, chemical oxidation, and biological degradation have been used [37]. Photocatalytic degradation [38], which uses semiconductor metal oxides as catalysts, is the favored technology because of its simplicity, high efficiency, and low cost. The photocatalytic degradation process comprises numerous phases, including light harvesting, exciton formation [39], OH radical generation via secondary reactions, and mineralization of organic contaminants by OH radical reactions [40]. On the other hand, Fast electron-hole recombination dramatically affects the efficiency of the process, resulting in a decrease in photocatalytic activity [41]. Several strategies such as metal or nonmetal doping, development of plasmonic structures, supporting the semiconductor metal oxides onto appropriate supports such as zeolites [42], and generating heterojunction by linking two or more semiconductors have been utilized to avoid or slow down this recombination [43].

However, a few methods were implemented to enhance the electrochemical as well as photocatalytic performance of transition metal-based materials, including heteroatom doping, defect introduction, and hierarchical structure creation [44]. By altering their internal components, catalysts' electronic structures can be effectively controlled in a particular way. The cation-cation interaction, which can obtain a modified d-d electronic structure and boost the movement of d electrons, has received much attention [45]. For instance, Deka et al. pointed out that adding Cu^{2+} to the $CuCo_2S_4$ crystal lattice can raise the concentration of Co^{3+} high-spin levels and result in exposed to high levels (111) facets, which encourages OER performance. According to Shen et al. research, the addition of the V component modifies the Co active center's electrical arrangement, further increasing the CoP's ability to water electrolysis [46]. The production of highly oxidized Co sites in HO-Co1-N_2 has also been demonstrated by Cao et al. [47], which facilitates the HER performance by improving water adsorption and dissociation. According to earlier findings, high-valence transition electrocatalysts (Co^{3+}, Ni^{3+}, V^{5+}etc.) have more open d electron orbits and are hence efficient at receiving electrons than low-valence metal catalysts. The ion species (O, N, S, P, and Se) present during electrocatalytic activity tend to absorb protons or water molecules, which is a significant point to consider [48]. The efficiency of the electrode material may be affected by the inversely associated cationic, e.g. and anionic s, pσ atomic orbitals. Despite this, a few thorough studies have demonstrated the usage of ionic species to modify electrocatalytic activity [49]. Developing highly efficient electrocatalysts will be facilitated by a complete understanding of the relationship between ionic species and electrocatalytic activity and by disclosing their electrochemical characteristics and relationships with intermediate electrocatalysts [20, 50]. In recent years, spinel $NiCo_2O_4$ has received much attention due to its outstanding electrochemical properties, unusual nanocomposite d orbitals, and remarkable corrosion resistance [51]. This spinel has shown excellent performance and stability for electrocatalytic activity. Therefore, we purposely convert the O to chalcogen components to produce the $CuScS_2$.

In contrast, spinel $CuScS_2$ is a substance that is especially promising for electrocatalytic OER owing to its considerable electrocatalytic performance, excellent durability, capacity to integrate transition metal oxides (CoO) into its lattice sites, and sustainability across a wide pH range [52]. The nano-structuring technique is an easy way to add more active sites with a lot of surface area and boost $CuScS_2$'s electrocatalytic activity. In order to create nanomaterials, many techniques are employed, such as hydrothermal, plasma imprinting, nano casting, thermal degradation, and many others. A nanocomposite material made of $CuScS_4$ and transition metal oxides plays a significant role in various fields [53]. The electronic state of $CuScS_2$ alters the binding energy of intermediate species in a way that lowers the electronic energy barrier and promotes good electrocatalytic activity[54].

We have here described a new type of bimetallic transition metal chalcogenide composite employing CoO, continuing the comparable trend. Here, we present the facile one-step hydrothermal synthesis of $CuScS_2$/CoO nanocomposites. From the fundamental ideas, it was observed that the composite $CuScS_2$/CoO demonstrated good morphology and it performed better against OER than its $CuScS_2$ and CoO analogue. The synthesized $CuScS_2$/CoO nanocomposite shows electrocatalytic activity with an OER overpotential of 179 mV@10 mA cm^{-2}. In all electrocatalytic studies, the obtained $CuScS_2$/CoO nanomaterials display better and more reliable electrochemical activity toward OER. On the other hand, the material was then employed for photocatalytic applications having a degradation efficiency of 92% with a reduced band gap of

2.91 eV. In comparison to typical electrocatalysts, the obtained nanomaterials demonstrated several benefits, including (1) low fabrication costs (as no noble metals are needed); (2) a simple one-step hydrothermal method; and (3) long-term durability over an extended period of time. The fact that we have looked into the properties of $CuScS_2$ and CoO and shown how they can be applied to enhance or improve the fundamental electrocatalytic activity of nanomaterials is more significant.

2. Experimental part

2.1 Chemical reagents

All of the chemicals were employed in their purest analytical form, and the suggested products were made using the following precursors: Sc(II) chloride ($ScCl_2$, Sigma Aldrich 99.8%), copper(II) acetylacetonate ($Cu(C_5H_7O_2)_2$, Sigma Aldrich 99.8%), Thiourea ($CS(NH_2)_2$, Sigma Aldrich 99.8%), ethanol (CH_3CH_2OH, Sigma Aldrich 99.8%), Cobalt acetate ($Co(CH_3COO)_2 \cdot 4H_2O$, Sigma Aldrich 99.5%) and polyethylene glycols ($H(OCH_2CH_2)_nOH$, Sigma Aldrich, 98.5%).

2.2 Synthesis of $CuScS_2$ nanoplates

In a 25 mL Teflon-lined stainless-steel autoclave, $ScCl_2$ (0.2 mM), the desired amount of copper (II) acetylacetonate (0.2 mM), and $CS(NH_2)_2$ (0.66 mM) were poured, and stirred for 10 min. To obtain a homogenous solution, 20 mL of ethanol was added to the autoclave and stirred again for 30 minutes. Afterwards, the autoclave was closed, kept at 220°C for 24 hours in an electric oven and then naturally cool at ambient temperature. The precipitates were gathered by centrifugation at 8000 rpm for 5 minutes, and the contaminants were then removed by twice-washing it with ethanol and deionized water. The final products were produced after a 24-hour drying process.

2.3 Synthesis of CoO nanoparticles

For the synthesis of CoO, the anhydrous ethanol (CH_3CH_2OH), polyethylene glycols 4000 (PEG 4000), and cobalt acetate were used, which were of analytical grade. In a typical response, the whole mixture was poured into 100 mL of Teflon-lined stainless-steel autoclave, which was used as a thermal reactor. After that, the autoclave was placed at 150 °C for 24 hours in an oven. Finally, the thermal reactor was cooled until it was at ambient temperature. The brownish-black insoluble solid ethanol products were separated by centrifugation and frequently rinsed with ethanol to get the pure product, and the resultant product was annealed at 450 °C to attain the CoO.

2.4 Fabrication of $CuScS_2$/CoO

In a 25 mL Teflon-lined stainless-steel autoclave, $ScCl_2$ (0.2 mM), a similar quantity of copper (II) acetylacetonate (0.2 mM), $CS(NH_2)_2$ (0.66 mM), and then the already generated CoO were also added in the reaction mixture. For the production of a homogenous solution, 20 mL of ethanol was added to the above reaction mixture and then stirred for 30 minutes. The autoclave was then closed and kept at 220°C for 24 hours in an electric oven before being allowed to cool gradually to ambient temperature. The residue was collected by centrifuging it at 8000 rpm for 5 minutes, and the contaminants were then removed by twice-washing it with ethanol and DI water. Finally, the ultimate products were produced after a 24-hour drying process.

2.5 Physical characterization

A Bruker D-2 powder diffractometer utilizing Ni-filtered with Cu-K radiations at a current of 10 mA under working conditions of 30 kV is used for the X-ray diffraction study. The 20–80° range was scanned at a rate of 5 $mVmin^{-1}$. All of the synthesized materials' structures were investigated using a scanning electron microscope with a Quanta 200-FEG. Using a JASCO-6800 with Fourier transform infrared (FTIR) spectroscopy, the surface functional group of the newly produced nanoparticles were identified. Brunauer Emmett Teller examined the specific surface area of each produced nanoparticle in order to better comprehend nitrogen adsorption-desorption-desorption (BET, Nova2200e Quanta chrome).

2.6 Fabrication of working electrode for OER

The functionalized electrocatalytic materials' working electrodes were created by drop-casting a slurry of newly created nanomaterials onto a piece of Ni-foam that had been cleaned and dried. Nickel foam was divided into uniform pieces (1 cm^2) and washed with a sonification method in 20 mL of DI water and ethanol for 30 minutes. The nickel foam was then washed with acetone and dried in an oven with a vacuum. The slurry was created by sonicating 100 μL of deionized water with a 10 mg manufactured catalyst for one hour. Then, 20 μL of catalytic ink was poured onto Ni-foam and allowed to dry. The oxygen evolution reaction (OER) via water electrolysis was studied using electrocatalyst/Ni-foam.

2.7 Electrochemical measurements

The electrochemical OER performances were conducted using electrochemical workstations (PGSTAT-204, Metrohm Autolab), cyclic voltammetry (CV), linear sweep voltammetry (LSV), electrochemical impedance spectroscopy (EIS), and chronoamperometry. These experiments were carried out in a pyrex glass cell shielded with Teflon using a standard three system with an electrode material deposited on nickel foam (1x 1 cm^2) acting as the working electrode, Pt wire as the counter electrode, and Ag/AgCl as the reference electrode in an alkaline environment (KOH solution) at ambient temperature. Before use, NF was thoroughly cleaned by sonification for 10 min in DI water, ethanol, and acetone. Aqua regia (HNO_3/HCl; 1:3) was used to boil the electrochemical cell to remove impurities before employing DI water and acetone. Following washing, it was dried for 1 hour at 80 °C in a drying oven. Before using Pt wire in an electrolytic cell, it was also cleaned with HNO_3 solution and then DI water. According to Eq. (1), all recorded potential values were examined about a reversible hydrogen electrode (RHE) [55].

$$E_{RHE} = E_{Ag/AgCl} + 0.059*pH + E^0 \tag{1}$$

Here, E_{RHE} stands for the potential of the hydrogen electrode, $E_{Ag/AgCl}$ for the potential of the Ag/AgCl electrode under study and pH for the electrolyte pH.

The following equation was used to compute the overpotential (η) for OER[56]:

$$\eta = E_{RHE} - 1.23 \tag{2}$$

Data from linear and cyclic voltammetry were gathered for the reaction kinetics with 50% IR-compensation at a scan rate of 5 mV s^{-1}. Prior to collecting all of the electrocatalytic results to ensure successful results, the electrolyte was bubbled with argon gas for 45 minutes to validate the absence of O_2 gas. In this instance, the geometric area (0.5 cm^2) of the NF (working electrode) was used to determine all current densities.

The electrocatalytic and dynamic performance reported in the following Eq 3. was examined using the Tafel slope method[57].

$$\eta = a + \frac{2.303RT}{\alpha nF}\log j \tag{3}$$

Where α denotes the charge transfer coefficient, n is the number of electrons involved in the reaction rates, η represents the overpotential value vs RHE, F stands for the Faraday constant, and j describes the current density at a particular overpotential value. The slope for the straight-line equation is represented as b.

The double layer capacitance, which is equivalent to the ECSA of the working electrodes as synthesized, was calculated using the non-faradaic zone in the cyclic voltammetry runs and analyzed at different scan speeds (10, 20, 30, 40, 50, and 60 mVs1) in 1.0 M KOH against RHE. For ECSA calculations, the specific capacitance (C_{sp}), which was taken into account as 0.04 $mFcm^2$ for an atomic scale flat planar surface electrode, was divided by the double layer capacitance (C_{dl}), which was determined using half of the slope of the plot (j vs. sweep range)[58].

$$\mathrm{ECSA} = \frac{\mathrm{Cdl}}{\mathrm{Cs}} \tag{5}$$

In the frequency range of 0.1 Hz to 100,000 Hz, the electrochemical impedance approach was used in 1.0 M KOH at an applied voltage of (0.5 V) vs Ag/AgCl. The Rct and Rs values were calculated using the NOVA 2.1 programmed (PGSTAT-204) by fitting the straightforward Randle’s circuit. This measurement was made over the duration of the entire investigation, and EIS provides a semicircle-shaped curve in the high-frequency zone and a straight edge in the low-frequency domain.

A good electrocatalyst should be active and also keep that activity going for a longer duration. Due to its excellent stability, it can effectively replace expensive catalysts, opening the door for its commercialization. Chronoamperometry can be used to confirm a nanomaterial's durability. For roughly 40 hours, the material's chronoamperometry was carried out at a potential of 0.8 V.

2.8. Photocatalytic study

To assess the photocatalytic efficiency of $CuScS_2/CoO$, a solution containing 100 mL of methylene blue was placed in a 500 mL Pyrex glass beaker under visible light (Tungsten bulb 200 W) using homemade photo-reactor. The $CuScS_2$, CoO, and $CuScS_2/CoO$ photocatalysts (0.1 g) were then added to the solution, and the mixture was stirred for 30 minutes to reach adsorption-desorption equilibrium. A 2 mL sample was extracted from the solution after 30 minutes of stirring in the dark, and its concentration was analyzed using a UV-visible spectrophotometer. Next, the suspension was exposed to sunlight/visible light and stirred continuously. Samples of the reaction mixture were collected every 15 minutes and analyzed using a UV-visible spectrophotometer to evaluate the photocatalytic activity, and the percent degradation efficiency was calculated using Co-Ct/Co *100, where Co is the initial concentration, Ct is the concentration of the dye concerning to the time under visible light irradiation.

3. Results and discussion

3.1. Structural and morphological characteristics

Powder X-ray diffraction (PXRD) patterns are used to examine the uniformity and crystallinity of as-produced catalytic materials, as shown in Fig. 1. CoO nanoparticles' PXRD pattern shows that the diffraction pattern is in strong agreement and fits the simulated CoO pattern well. The cubic structure with the (111), (200), (220), (311), and (222) planes at $2\theta = 36, 42, 61, 72$, and 77°, respectively, correlate to the diffraction pattern of crystalline CoO (Fig. 1). Similar to this, the $CuScS_2$ PXRD pattern demonstrated that all diffraction patterns are indexed to $CuScS_2$ as shown in Fig.1 shows prominent $CuScS_2$ peaks that can be assigned to the following planes/angles: (100)/27°, (101)/31°, (102)/40°, (003)/44°, (110)/48°, (013)/53°, (200)/56°, (022)/65°, (113)/68° and (203)/74, it shows that pattern of $CuScS_2$ matched well with the available simulated pattern of $CuScS_2$. The $CuScS_2$ PXRD patterns further show that no additional peaks for impurities are seen, indicating that these samples were formed in a single phase and with a high degree of purity. Additionally, it was found that the pattern of $CuScS_2$/CoO sustained its crystalline structure, remained unaltered, and retained the dominance of both phases, like $CuScS_2$ and CoO synthesis, confirming the successful synthesis of the products.

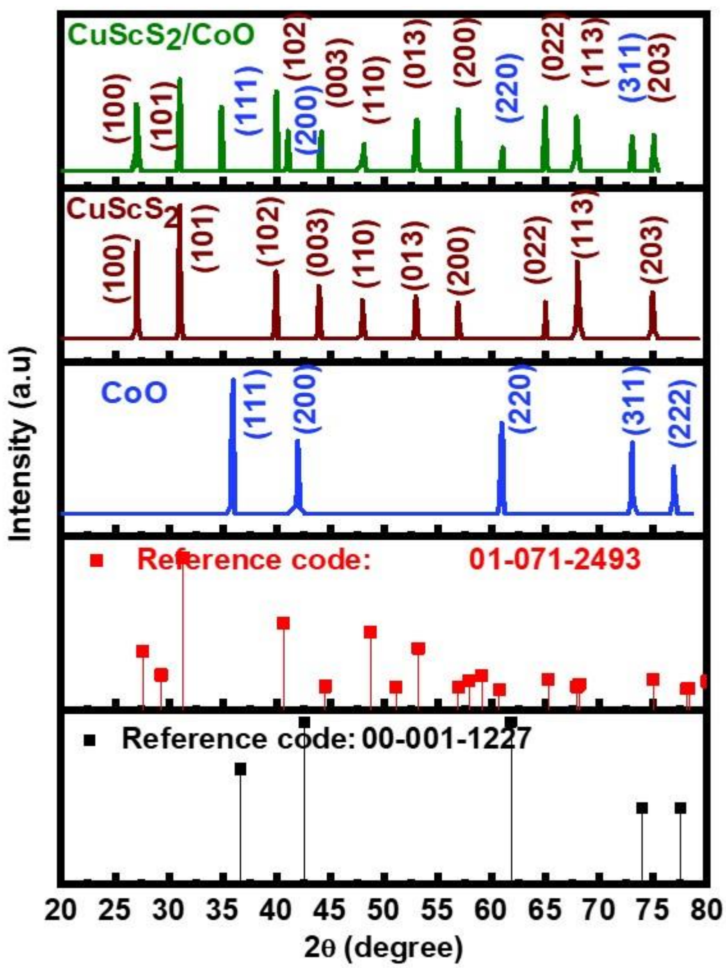

Fig. 1: XRD patterns of all synthesized materials like $CuScS_2$, CoO, and $CuScS_2$/CoO nanocomposite

A further investigation using Fourier transform infrared (FTIR) spectroscopy is made into the production and appropriate incorporation of CoO nanoparticles into $CuScS_4$. The FT-IR spectra of each synthesized sample are shown in Fig. 2. The CoO vibrations cause a characteristic absorption peak in the FTIR spectra at 764 cm^{-1} [59] which is due to Co-O vibration. The vibrational frequencies of the H-O and C-O-C functional groups were present from the adsorbed H_2O and CO_2 molecules on the surface of the entire product at 2375 and 3341 cm^{-1} [60]. The prepared sample $CuScS_2$'s FTIR spectrum is shown in Fig.2. The Cu-Sc, Sc-S, and CuS bands from the constructed heterostructure molecule of $CuScS_4$ can be ascribed to the vibration frequencies of the observed strong peaks at 678, 784, and 882 cm^{-1}. The bands between 400 and 800 cm^{-1} in the $CuScS_2$/CoO FTIR spectrum relate to the typical bending vibration of Cu-Sc, Sc-S, and Cu-O at 678, 882, and 764 cm^{-1}, respectively [61, 62]. The existence of these bands demonstrated the production efficiency of the produced nanostructure.

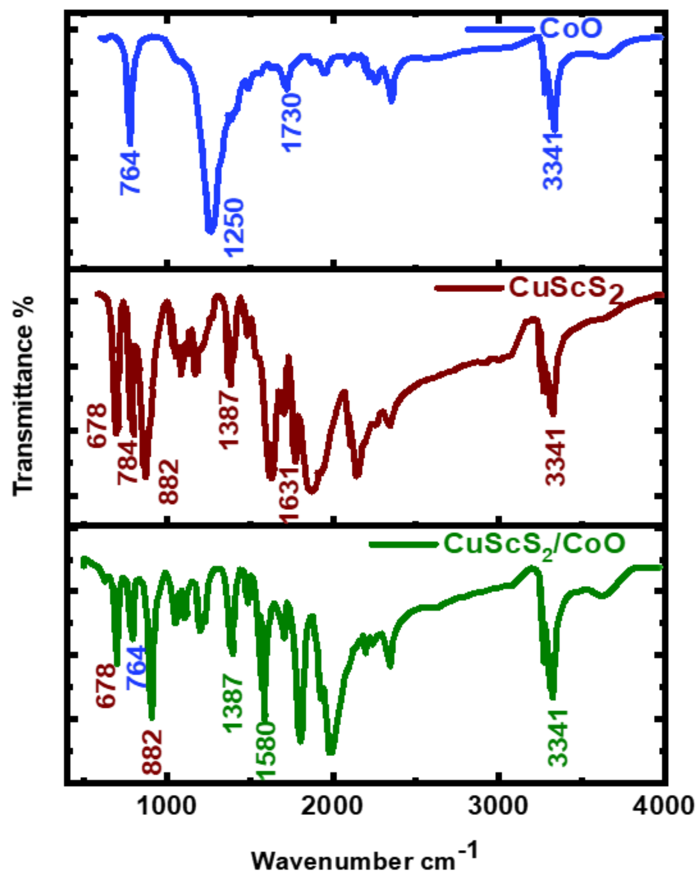

Fig. 2: FTIR spectrum of CoO, $CuScS_2$ and $CuScS_2/CoO$ nanocomposite

Scanning electron microscopy (SEM) analysis was used to assess the morphology and content of all the produced samples. The SEM images of CoO, $CuScS_2$ and $CuScS_2/CoO$ are shown in fig. 3 (a-c), respectively. The CoO has developed into uniform distribution crystals with irregular round shapes, as shown in fig. 3(a). The $CuScS_2$ has developed into well-defined block-shaped particles, as illustrated by the SEM image (Fig. 3b). Furthermore, the SEM image of $CoScS_4/CoO$ nanocomposite was shown in fig. 3c and d revealed SEM micrographs indicating the formation of the nanocomposite, demonstrating the presence of both phases, which were helpful for the easy transfer of electrons during the photochemical as well as the electrochemical reaction.

TEM pictures show the insight view of $CuScS_2/CoO$ nanocomposite showing the morphology, which is compatible with SEM images of the freshly exposed surface, which show defined boundaries as shown in fig. 3 e and f at low and high magnification. Furthermore, this type of morphology leads to a considerable increase in specific surface area and permeability within the resultant fabricated materials. These interrelated features causing more active sites that contribute to higher OER activity.

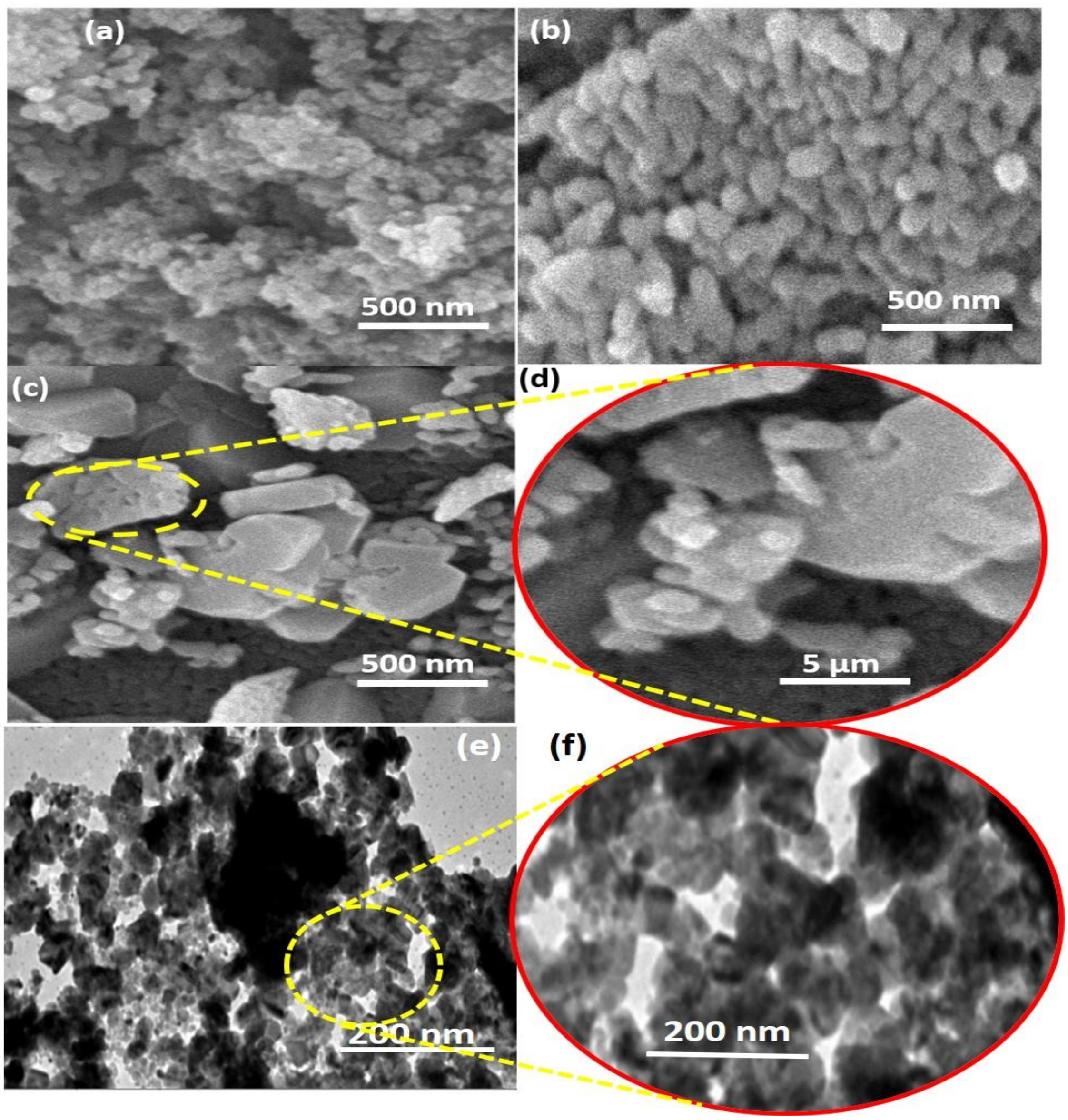

Fig. 3: SEM image of a) CoO, b) $CuScS_2$, and c-d) $CuScS_2$/CoO nanocomposite, (e-f) TEM micrograph of the nanocomposite at low and high magnification.

The elemental compositions of the produced materials were determined using energy dispersive spectroscopy (EDS). Figure 4 (a-c) depicts the distribution of all elements present in the fabricated material like CoO, $CuScS_4$ and the nanocomposite materials.

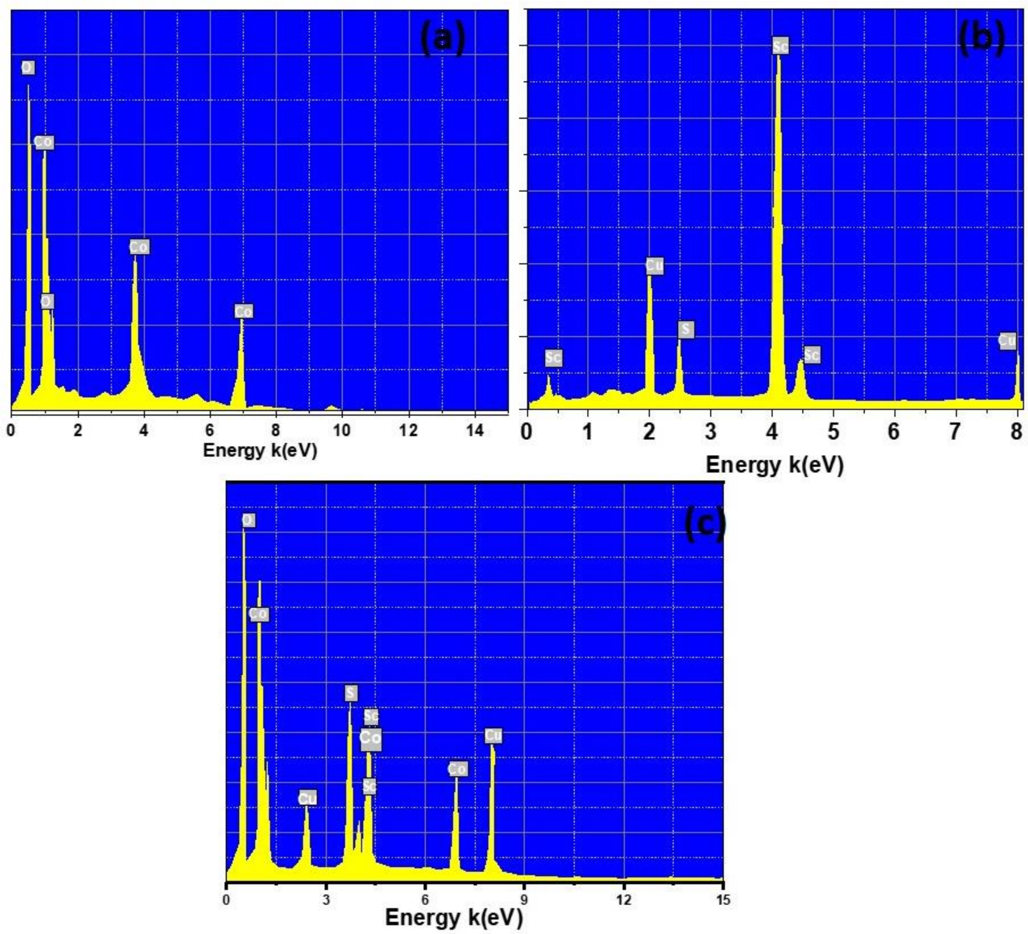

Figure 4: EDX spectrum of (a) CoO, (b) $CuScS_4$, and (c) nanocomposite materials.

The nitrogen adsorption/desorption isotherm (777 K), as well as the pore size distribution analysis, were used to evaluate the textural characteristics of all the manufactured materials, as shown in fig. 5(a-b). The CoO, $CuScS_2$, and $CuScS_2$/CoO have BET surface areas of 23, 39, and 54.7 m^2/g

and pore volumes of 0.33, 0.49, and 0.54 cm^3, respectively. The resultant BET isotherm shows type-IV with mesoporous nature, having much active sites on the surface of the fabricated materials because they have better active sites on the surface, because the electrode materials with bigger surface areas typically have better efficacy for the transportation of electrons.

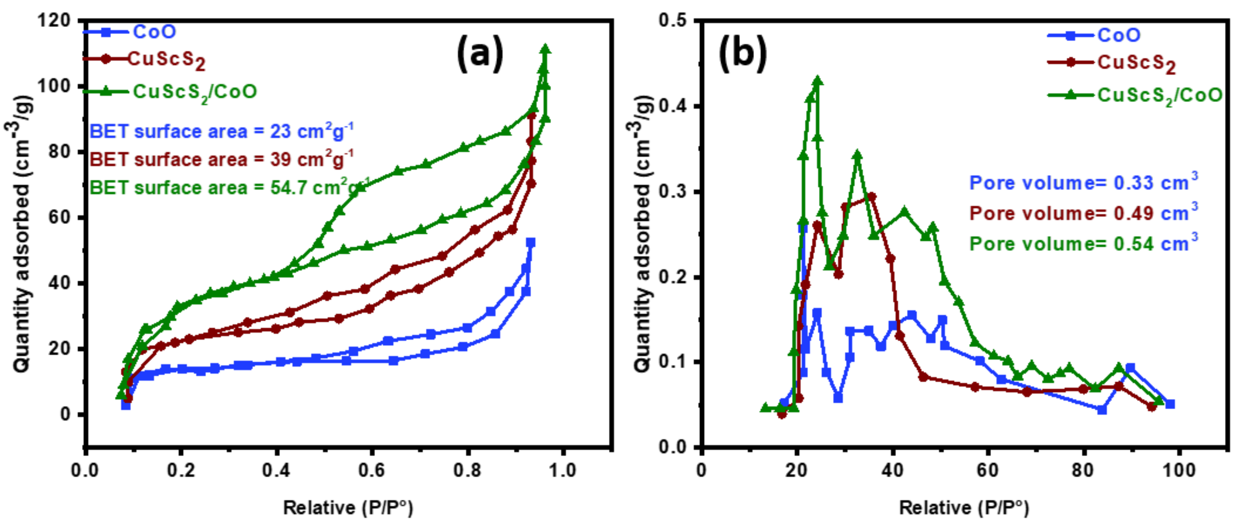

Fig. 5: a) BET isotherm, b) pore size distribution of CoO, $CuScS_2$, and CoO/$CuScS_2$ nanocomposite.

Figure 6 (a-c) displays the UV-visible DRS spectra of CoO, $CuScS_2$, and $CuScS_2$/CoO, which reveal that the formation of the nanocomposite shifts the light absorption capacity towards the longer wavelength region. CoO exhibits an absorption peak in the UV range at 240 nm, attributed to its wide bandgap. $CuScS_2$ structure improves the visible light absorption due to its photosensitizing effect, using tauc's plot and by extrapolating the horizontal and steeply increasing segments of the curves at the intersection of wavelength, the absorption peaks for $CuScS_2$ and $CuScS_2$/CoO were identified at 340 and 446 nm, respectively. The bandgaps for CoO, $CuScS_2$, and $CuScS_2$/CoO were determined as 2.75, 2.3 eV and 1.55 eV, respectively as depicted in fig. 6d-f, indicating that the nanocomposite ($CuScS_2$/CoO) has a smaller band gap to control the electron-hole recombination process. Therefore, $CuScS_2$/CoO can be utilized as an effective photocatalyst under visible light for the degradation of organic pollutants (methylene blue).

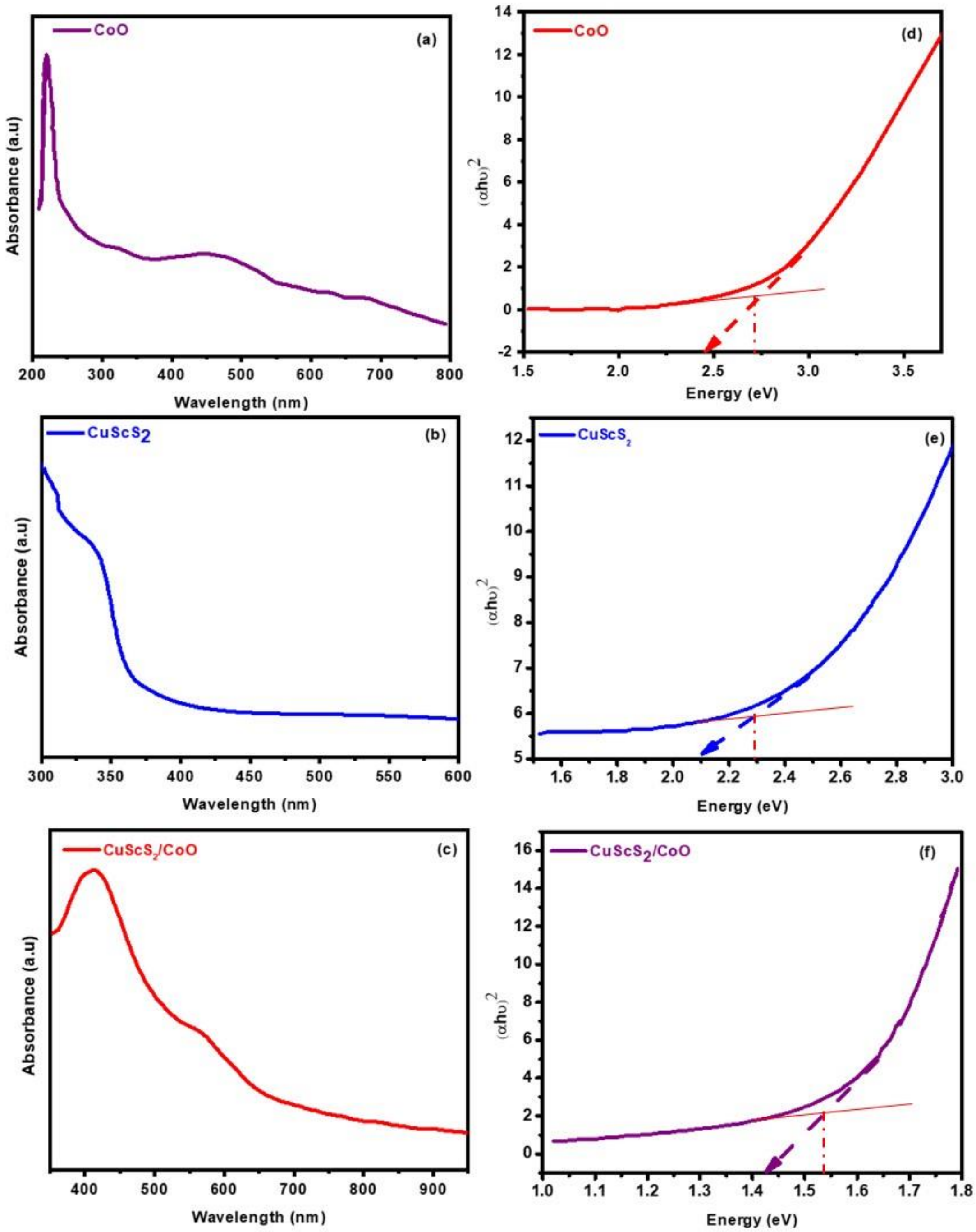

Fig. 6: a-c) UV visible absorption spectra, (d-f) Tauc plot for band gap calculation

3.2. Electrochemical measurements

For the oxygen evolution reaction, a three-electrode system was modified to test the OER electrochemical performance of the produced CoO, $CuScS_2$, and $CuScS_2$/CoO electrocatalysts. As shown in Fig. 7 (a,b), CV and LSV were used to characterize the OER efficiency of CoO, $CuScS_2$, RuO_2, and $CuScS_2$/CoO measured at a scan rate of 5 mV s^{-1}. To achieve a current density of 10 mA cm^{-2} and 100 mA cm^{-2}, CoO, $CuScS_4$, RuO_2, and $CuScS_2$/CoO exhibit the onset potential and overpotential listed in Table 1. Because of the synergistic impact of $CuScS_2$/CoO heterostructure, $CuScS_2$/CoO has a lower onset and overpotential than individual CoO and $CuScS_2$ in this situation. The improved OER performance of the $CuScS_2$/CoO electrode material may also result from the $CuScS_2$/CoO heterostructure's reduced nuclei production and good morphology, as well as high BET surface area.

Table 1: Comparison of Overpotential, Onset potential and Tafel slope for CoO, $CuScS_4$, RuO_2, and $CuScS_2$/CoO nanocomposite.

Materials	**Overpotential (mV) at 10 mA cm^{-2}**	**Overpotential (mV) at 100 mA cm^{-2}**	**Onset Potential V**	**Tafel slope mV dec^{-1}**
CoO	242	440	1.45	83
$CuScS_2$	201	399	1.42	65
RuO_2,	248	330	1.43	-
$CuScS_2$/CoO	179	297	1.41	46

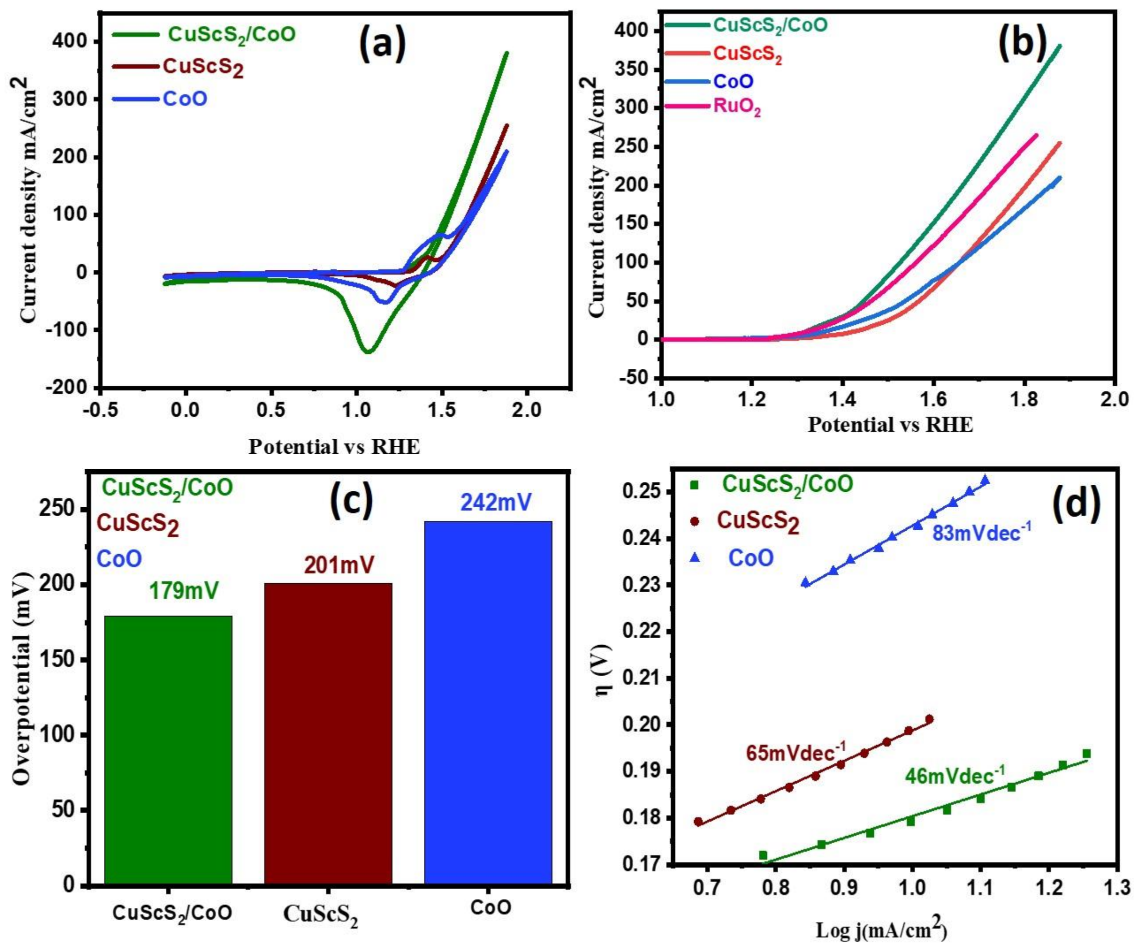

Fig. 7: (a) CV polarization curves of all synthesized materials (b) LSV curves (c) Comparison of Overpotential CoO, $CuScS_2$, RuO_2, and $CuScS_2$/CoO composites (d) Tafel slope

In order to investigate the dynamics by fitting the linear sections, Tafel plots of all the synthesized materials were additionally obtained by polarization curves (Fig. 7d). The OER is a complicated multistep proton/coupled reaction, hence it is essential to calculate Tafel values using a specific kinetic approach. Surface roughness homogeneity, intrinsic resistance, and variance in the charge transfer coefficient all have an impact on the Tafel value. On the other hand, electron transfer might be a practical technique to get details regarding the OER electrocatalytic effectiveness. A lower Tafel value suggests a reduced overpotential requirement for the electrocatalyst to reach a higher current density. In Table 2, the observed Tafel slopes for CoO, $CuScS_2$, and composites of $CuScS_2$ and CoO are listed. The $CuScS_2/CoO$ (46 mV dec^{-1}) composite has a much lower Tafel slope value compared to CoO (83 mV dec^{-1}) and $CuScS_2$ (65 mV dec^{-1}), demonstrating a faster rate of electron transport. The $CuScS_2/CoO$ heterostructure consequently exhibits a remarkable synergistic impact and a lower Tafel slope as a result. Due to its conductivity, Cu, Sc, and Co have typically been suggested as effective electrode materials for OER.

The following details the potential O_2 evolution mechanism of $CuScS_2/CoO$. The $CuScS_2/CoO$ electrode surface oxidized to Cu^{+2}, Co^{+2} and Sc^{+2} during coordination in an alkaline solution, leading to the formation of metal hydroxides and oxides, i.e., MOOH (where M=Co, Cu and Sc), and the ensuing oxidized Cu^{+2}, Co^{+2} and Sc^{+2} ions catalyze the oxidative water reaction related to metal oxides and hydroxides in alkaline media to produce OERs. As a result, the deprotonation associated with the active sites during the production of intermediates (oxyhydroxide) leads to a quick evolution of oxygen [63]. $CuScS_2$/ CoO's hypothesized OER process is assumed as.

$$M + OH^- \rightarrow M\text{–}OH^- + e^- \quad (6)$$

$$M\text{–}OH^- + OH^- \rightarrow M\text{–}O + H^+ + e^- \quad (7)$$

$$M\text{–}O + OH^- \rightarrow M\text{–}OOH + e^- \quad (8)$$

$$M\text{–}OOH + OH\text{-} \rightarrow M + O_2(g) + H^+ + e^- \quad (9)$$

The double-layer capacitance was measured to do the electrochemical experiments for the OER process. Five CV scans (30-90 mV/s) with scan intervals of 5 mV s^{-1} each were carried out in the non-Faradaic region's small window (Fig. 8a–c). The roughness factor, Faradaic current attribution, and porousness of the catalyst can all cause the CV curves to break at some time. By setting j against the sweep rate, the results from the CV scan were then used to calculate the slope. The slope was determined to be 0.0028, 0.0045, and 0.010 mF/cm^2, respectively, for pure CoO, $CuScS_4$, and $CuScS_2$/CoO. The comparable Cdl values for CoO, $CuScS_2$, and $CuScS_2$/CoO are 0.0014, 0.0025, and 0.005 mF/cm^2, respectively (Fig. 8 (d-f)). Electrocatalyst specific area (ECSA) was calculated by dividing each Cdl value by the surface-normalized specific resistance. For the aforementioned electrocatalysts, the ECSA was computed as 0.35, 0.625, and 1.25 cm^2 for CoO, $CuScS_4$, and $CuScS_2$/CoO nanocomposite, respectively.

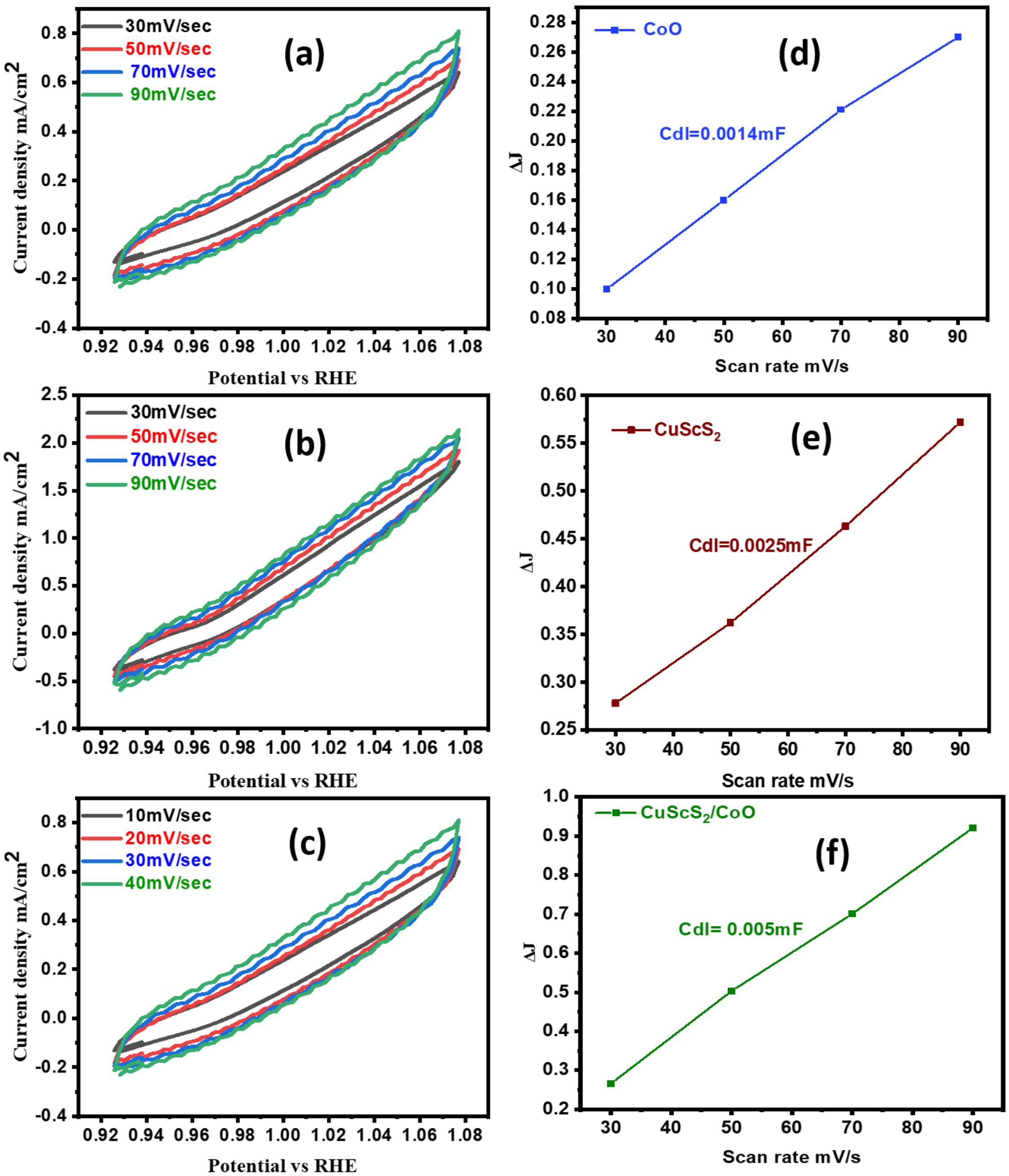

Fig. 8: CV curves (a) CoO, (b) $CuScS_4$ and (c) $CuScS_2$/CoO (d-f) Cdl of CoO, $CuScS_2$ and $CuScS_2$/CoO nanocomposite.

For EIS, the electrocatalytic workstation was also equipped with Nova 2.1 software to test the electrocatalytic performance of the synthesized electrode materials in the frequency range of 10 to 100 kHz. Fig. 9 shows the Nyquist plot for CoO, $CuScS_4$, and $CuScS_2$/CoO electrode with Randle's circuit inset. Due to its lower diffusion resistance, excellent capacitive properties, and greater electrochemical surface area, the $CuScS_2$/CoO manufactured electrode exhibits the shortest semicircle of any electrode compared to pure nanomaterial. These results suggest that the abundant oxyhydroxide active sites that are easily absorbed onto the contact surface of the electrode material with the electrolyte, favoring the electrocatalytic OER, may be responsible for the considerably higher charge transport potential of the synthesized $CuScS_2$/CoO electrode at 0.5 V.

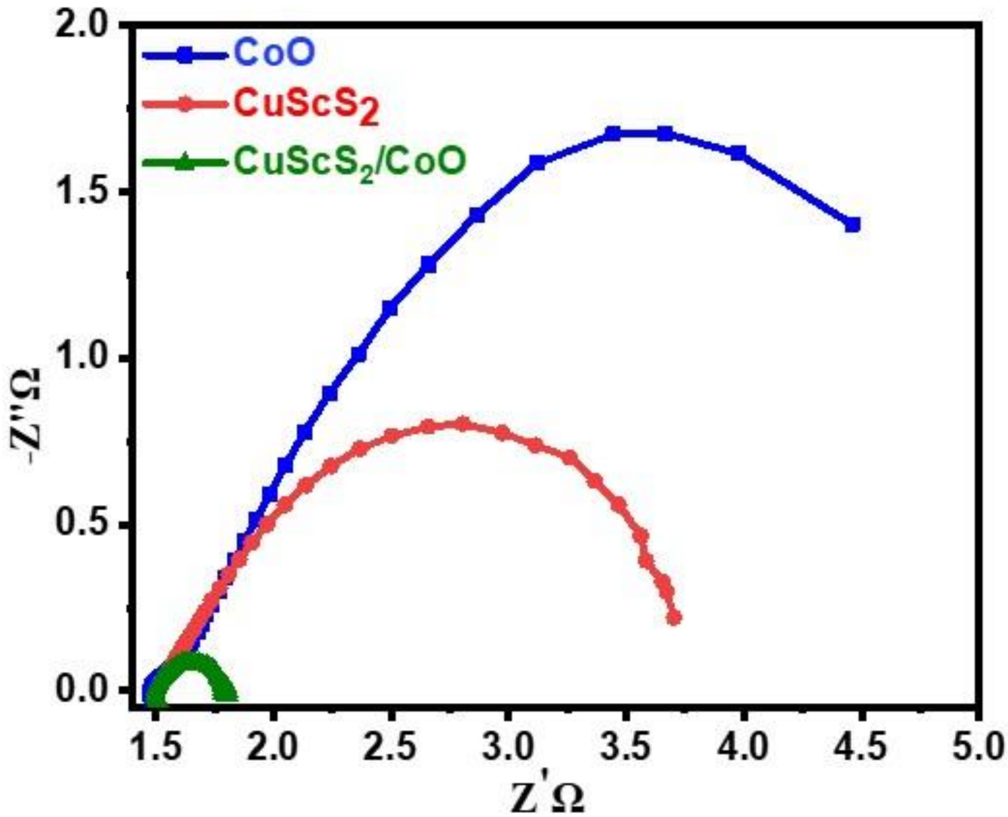

Fig.9: EIS Nyquist plots for all the synthesized electrocatalysts.

Table 2: Comparative study with other reported results.

Serial.No	Electrocatalyst	Substrate	Electrolyte	Overpotential (mV)	References
1	CoNiSe/NC	Carbon Cloth	1 M KOH	270	[64]
2	$NiCo_2Se_4$	Glassy Carbon	1 M KOH	300	[65]
3	$NiCoSe_2$	Glassy Carbon	0.1 M KOH	360	[66]
4	$NiCo_2O_4$	Glassy Carbon	0.1 M KOH	430	[67]
5	N, Fe-NiSe@NIF	Ni/Fe-alloy	1 M KOH	232	[67]
6	$CoSe_2/FeSe_2$	Ni Foam	1 M KOH	240	[68]
7	$Co_3Se_4/FeSe_2$				[69]
8	$Ni_{1-x}CoxSe_2$-y-OOH	Carbon Fiber Paper	1 M KOH	233	[70]
9	$Ni_{1-x}Co_xSe_2$	Graphite Foil	1 M KOH	264	[71]
10	$Fe_{40}Co_{40}Se_{40}$	Carbon Fiber Paper	1 M KOH	307	[72]
11	$NiSe/Ni_3Se_2$/NF	Ni foam	1 M KOH	260	[73]
12	**$CuScS_2$/CoO**	**Ni foam**	**1 M KOH**	**179**	**This work**

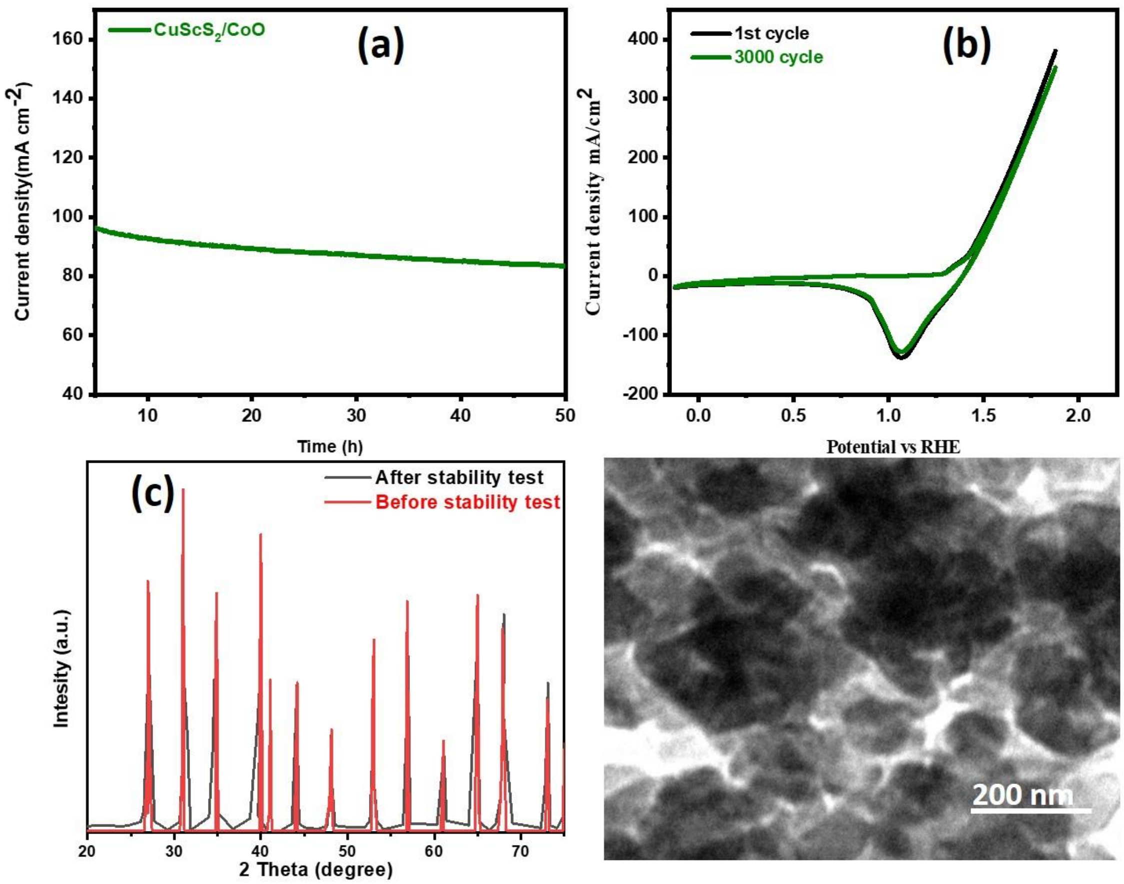

Fig.10: (a) Chronoamperometry of the nanocomposite (b) CV cycles, (c) XRD after stability test, and (d) TEM micrograph of the nanocomposite.

Furthermore, the lifespan and durability of electrocatalysts are important factors in the development of low-cost and extremely effective electrocatalysts for OER. Chronoamperometric measurements were carried out for 25 hours at the appropriate static potential vs RHE to test the electrocatalysts' stability. The amperometry i-t plot of the $CuScS_2/CoO$ nanocomposites is shown in Fig. 10a, and it shows that the electrocatalyst has unusually high durability and steady-state oxidative potential without any appreciable changes in the current density up to 50 hours. Fig. 10b shows the CV polarization curves for $CuScS_2/CoO$ electrocatalyst before and after 3000 CV cycles at a 10 mV s^{-1} scan rate, respectively. Additionally, Fig. 10b shows minor variations in the first and 3000 cycles, indicating that the OER keeps its electrochemical performance for a longer period of time. Fig. 10 c and d represents the XRD and TEM micrograph of the nanocomposite after the stability test to confirm the structural and morphological analysis. The resultant analysis show a little change in the peaks intensities of the XRD pattern but the peaks position remained at same 2-theta indicating that the composite material has good structural stability while the agglomerations can be seen on the surface after stability which may be due to the adsorption of various species on its surface. Hence, in this study the $CuScS_2/CoO$ composite's higher electrocatalytic activity than pure $CuScS_2$ and CoO can be due to synergistic interactions between their close proximity, complementing characteristics, and also the composite possesses a clearly defined heterostructure with higher surface area that enables effective charge transfer between $CuScS_2$ and CoO. As a result, several active sites are created, and reactants can be adsorbate and activated on the surface of the fabricated materials. For the necessary electrocatalytic process, $CuScS_2/CoO$ has a lower onset potential and a larger current density, which can be attributed to improved conductivity and optimal energetics at the interface, according to electrochemical investigations. It is shown that $CuScS_2/CoO$ have the potential to be used as electrocatalysts for a variety of processes by utilizing their natural catalytic capabilities to enhance reaction kinetics and overall performance.

Photochemical study

Fig. 11 (a-c) depicts the UV graphs to conform the photocatalytic activity of the as-prepared photocatalysts towards the photodegradation of methylene blue under visible light. To compare the photocatalytic activity of pure CoO, $CuScS_4$, and $CuScS_2/CoO$, photodegradation tests were done by irradiating 100 mg L^{-1} solutions of methylene blue and 0.1 g of the catalyst at room temperature for 80 minutes under visible light. Prior to irradiation, the catalyst and methylene blue solution were magnetically swirled for 30 minutes in the dark to achieve equilibrium between adsorption and desorption. A blank experiment was also conducted by swirling the pure dye solution for one hour without a catalyst. $CuScS_2$/CoO samples had more photocatalytic activity than pure $CuScS_2$ and CoO. In the presence of pure CoO, $CuScS_4$, and $CuScS_2$/CoO nanocomposite, the elimination percentages of methylene blue were determined to be 36%, 46%, and 92%, respectively, as depicted in fig. 11d. The decreased photocatalytic activity of CoO can be due to its large bandgap (2.49 eV), which hinders the production of excitons when illuminated with visible light.

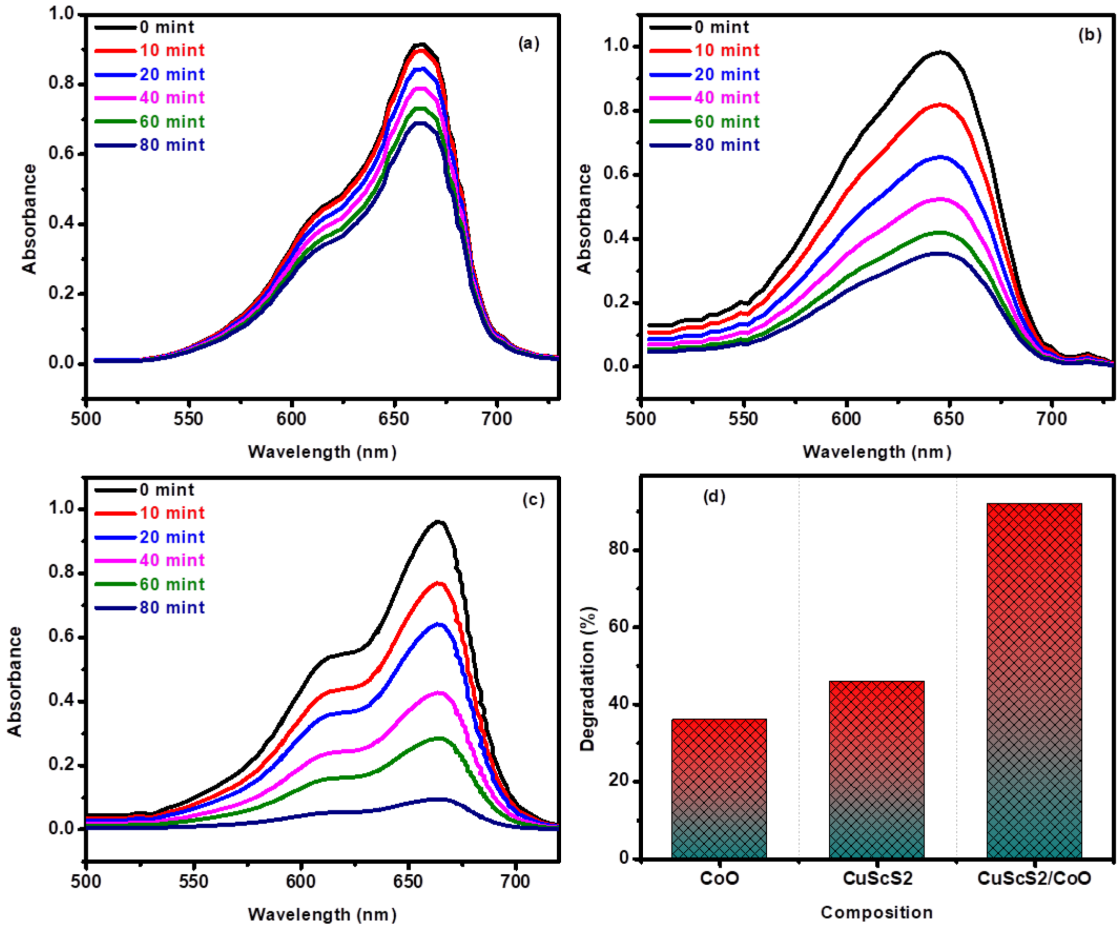

Fig. 11: (a-c) Absorbance spectra, d) degradation (%) of CoO, $CuScS_4$, and $CuScS_2$/CoO nanocomposite.

The positions of the valance and the conduction bands have been calculated using following equation:

$$ECB = X - E^c - 0.5E_g$$

$$EVB = X - E^c + 0.5E_g$$

Where ECB and EVB are the edge potentials of the conduction and valance bands, respectively, and X is the geometric mean electronegativity of the constituent elements. The X values of CoO and CuScS2 are 1.56 and 2.10, respectively. E^c is the energy of unconstrained electrons on the hydrogen scale (4.5 eV), and E_g is the bandgap energy. Based on the Tauc graphs in Figure 6(d-e), the Eg values of CoO and CuScS2 were determined to be 2.75 eV and 2.3 eV, respectively. The CoO and CuScS2 ECB values were calculated and found to be -4.31 eV and -3.55 eV, respectively, whereas EVB values were -1.57 eV and -1.25 eV. The energy diagram has been built based on the calculated values of the valance and conduction band potential edges illustrated in Fig. 12. Photogenerated electrons from the CoO conduction band may be easily transported to the $CuScS_2$ conduction band, reducing hole and electron recombination, as shown in Fig. 12. The decrease in e/h+ pair recombination boosted the photocatalytic effectiveness of the nanocomposite. Hence, oxygen molecules in the dye solution coupled with electrons to generate superoxide radical ($\bullet O_2$), whereas holes mixed with H_2O to generate hydroxyl radical (•OH) [74-76]. The holes at the VB of CoO immediately oxidized MB, and the powerful oxidant radicals •OH and $\bullet O_2$ destroyed the MB molecule effectively. The following is our suggested mechanism for the degradation of MB by $CuScS_2$/CoO in the presence of sunshine.

$$CuScS_2/CoO + hv \rightarrow CuScS_2/CoO\ (e_{CB}^{-} + h_{VB}^{+}) \qquad (1)$$

$$e^{-}(CB) + O_2 \rightarrow {}^{\bullet}O_2^{-} \qquad (2)$$

$$h^{+}(VB) + OH^{-} \rightarrow {}^{\bullet}OH \qquad (3)$$

$${}^{\bullet}O_2^{-} + MB \rightarrow \text{products (degraded)} \qquad (4)$$

$${}^{\bullet}OH + MB \rightarrow \text{products (degraded)} \qquad (5)$$

$$h^{+}(VB) + MB \rightarrow \text{Final products} \qquad (6)$$

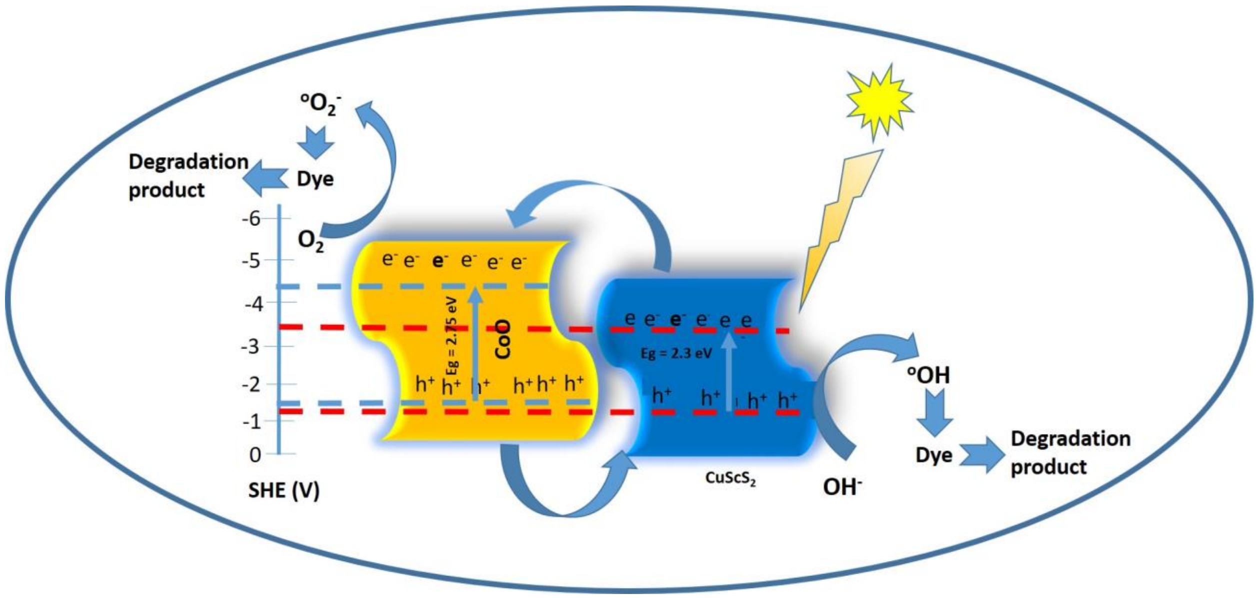

Fig. 12: Schematic illustration of the photocatalytic mechanism

Summary

To summarize, the $CuScS_2/CoO$ nanocomposite was synthesized using a hydrothermal method. Furthermore, the structure, morphology, and performance were evaluated using various analytical techniques. The $CuScS_2/CoO$ nanocomposite exhibits excellent OER efficiency, with a low overpotential of 179 mV and a reduced Tafel slope of 46 mV dec^{-1}. The lower Tafel slope of the $CuScS_2/CoO$ nanocomposite promotes the OER reaction by facilitating ion exchange through the formation of oxygen vacancies in the nanostructure, which provides a large surface area. The synergy between CoO and $CuScS_2$ also enhances the flow of electrons, further improving the efficiency of the OER reaction. The composite material also showed good photocatalytic activity of 92 % degradation efficiency under visible light. To summarize, the $CuScS_2/CoO$ nanocomposite demonstrates superior oxygen electrode performance in aqueous electrolytes for hydrogen fuel production by water electrolysis compared to other nanomaterials and used for water treatment. This method of creating nanomaterials with unique morphologies can be used to improve the various electrochemical properties, such as photoelectrochemical and electrocatalytic performance, among others.

Acknowledgment:

This work was funded by the Researchers Supporting Project Number (RSP2023R243) King Saud University, Riyadh, Saudi Arabia.

References

[1] W. Steffen, P.J. Crutzen, J.R. McNeill, The Anthropocene: are humans now overwhelming the great forces of nature, Environment and Society, 36 (2007) 614-621.
[2] S.B. Eaton, M. Konner, M.J. Shostak, Stone agers in the fast lane: chronic degenerative diseases in evolutionary perspective, American Journal of Medicine, 84 (1988) 739-749.
[3] E.A. Wrigley, Energy and the English industrial revolution, Philosphical Transactions of Royal Society, 371 (2013) 20110568.
[4] H. Xue, H. Gong, Y. Yamauchi, T. Sasaki, R. Ma, Photo-enhanced rechargeable high-energy-density metal batteries for solar energy conversion and storage, Nanoreserach Energy, 1 (2022) e9120007.
[5] Z.P. Cano, D. Banham, S. Ye, A. Hintennach, J. Lu, M. Fowler, Z.J. Chen, Batteries and fuel cells for emerging electric vehicle markets, Nature Energy, 3 (2018) 279-289.
[6] A. Dehghani-Sanij, E. Tharumalingam, M. Dusseault, R.J. Fraser, Study of energy storage systems and environmental challenges of batteries, Renewable and Sustainable Energy Review, 104 (2019) 192-208.
[7] A. Ursua, L.M. Gandia, P. Sanchis, Hydrogen production from water electrolysis: current status and future trends, Proceedings of the IEEE, 100 (2011) 410-426.
[8] A. Nicita, G. Maggio, A. Andaloro, G. Squadrito, Green hydrogen as feedstock: Financial analysis of a photovoltaic-powered electrolysis plant, International Journal of Hydorgen Energy, 45 (2020) 11395-11408.
[9] W.T. Hong, M. Risch, K.A. Stoerzinger, A. Grimaud, J. Suntivich, Y. Shao-Horn, Toward the rational design of non-precious transition metal oxides for oxygen electrocatalysis, Energy & Environmental Science, 8 (2015) 1404-1427.
[10] L.-W. Chen, H. Liang, Ir-based bifunctional electrocatalysts for overall water splitting, Catalysis Science & Technology, 11 (2021) 4673-4689.
[11] E. Zoulias, E. Varkaraki, N. Lymberopoulos, C.N. Christodoulou, G. Karagiorgis, A review on water electrolysis, Tcjst, 4 (2004) 41-71.
[12] M. Yue, H. Lambert, E. Pahon, R. Roche, S. Jemei, D.J. Hissel, Hydrogen energy systems: A critical review of technologies, applications, trends and challenges, Renewable and Sustainable Energy Reviews, 146 (2021) 111180.
[13] K. Zeng, D.J. Zhang, Recent progress in alkaline water electrolysis for hydrogen production and applications, Progress in Energy and combustion Science, 36 (2010) 307-326.
[14] J. Yu, T.A. Le, N.Q. Tran, H. Lee, Earth-abundant transition-metal-based bifunctional electrocatalysts for overall water splitting in alkaline media, Chemsitry-A European Journal, 26 (2020) 6423-6436.

[15] J. Wang, X. Yue, Y. Yang, S. Sirisomboonchai, P. Wang, X. Ma, A. Abudula, G. Guan, Earth-abundant transition-metal-based bifunctional catalysts for overall electrochemical water splitting: A review, Journal of Alloys and Compounds, 819 (2020) 153346.
[16] Y. Wu, Y. Li, T. Zhao, X. Wang, V.I. Isaeva, L.M. Kustov, J. Yao, J. Gao, Bimetal-organic framework-derived nanotube@ cellulose aerogels for peroxymonosulfate (PMS) activation, Carbohydrates Polymers, 296 (2022) 119969.
[17] X. Xue, J. Zhong, J. Liu, Z. Hou, X. Wu, S. Li, M.J. Yu, Hydrolysis of metal-organic framework towards three-dimensional nickel cobalt-layered double hydroxide for high performance supercapacitors, Journal of Energy Storage, 31 (2020) 101649.
[18] W.-D. Zhang, H. Yu, T. Li, Q.-T. Hu, Y. Gong, D.-Y. Zhang, Y. Liu, Q. Fu, H. Zhu, X. Yan, Hierarchical trimetallic layered double hydroxide nanosheets derived from 2D metal-organic frameworks for enhanced oxygen evolution reaction, Applied Catalysis B, 264 (2020) 118532.
[19] Z.Y. Yu, Y. Duan, X.Y. Feng, X. Yu, M.R. Gao, S. Yu, Clean and affordable hydrogen fuel from alkaline water splitting: past, recent progress, and future prospects, Advanced Materials, 33 (2021) 2007100.
[20] L. Han, S. Dong, E. Wang, Transition-metal (Co, Ni, and Fe)-based electrocatalysts for the water oxidation reaction, Advanced Materials, 28 (2016) 9266-9291.
[21] W. Jin, G.J. Maduraiveeran, Recent advances of porous transition metal-based nanomaterials for electrochemical energy conversion and storage applications, Materials Today Energy, 13 (2019) 64-84.
[22] Y. Li, Y. Wu, T. Li, M. Lu, Y. Chen, Y. Cui, J. Gao, G. Qian, Tuning the electronic structure of a metal–organic framework for an efficient oxygen evolution reaction by introducing minor atomically dispersed ruthenium, carbon Energy, 5 (2023) e265.
[23] M. Yu, E. Budiyanto, H. Tüysüz, Principles of water electrolysis and recent progress in cobalt-, nickel-, and iron-based oxides for the oxygen evolution reaction, Angewandte Chemie International Edition, 61 (2022) e202103824.
[24] M.S. Burke, M.G. Kast, L. Trotochaud, A.M. Smith, S.W. Boettcher, Cobalt–iron (oxy) hydroxide oxygen evolution electrocatalysts: the role of structure and composition on activity, stability, and mechanism, Journal of American Chemical Society, 137 (2015) 3638-3648.
[25] X. Li, J. Wang, Phosphorus-based electrocatalysts: black phosphorus, metal phosphides, and phosphates, Advanced Materials Interfaces, 7 (2020) 2000676.
[26] G. Zhang, L. Jin, R. Zhang, Y. Bai, R. Zhu, H. Pang, Recent advances in the development of electronically and ionically conductive metal-organic frameworks, Coordination Chemistry Reviews, 439 (2021) 213915.
[27] F. Liao, X. Zhao, G. Yang, Q. Cheng, L. Mao, L. Chen, Recent advances on two-dimensional NiFe-LDHs and their composites for electrochemical energy conversion and storage, Journal of Alloys and Compounds, 872 (2021) 159649.
[28] G. McMullan, C. Meehan, A. Conneely, N. Kirby, T. Robinson, P. Nigam, I. Banat, R. Marchant, W. Smyth, Microbial decolourisation and degradation of textile dyes, Applied microbiology and biotechnology, 56 (2001) 81-87.
[29] B. Singh, N. Sharma, Mechanistic implications of plastic degradation, Polymer degradation and stability, 93 (2008) 561-584.
[30] W. Zhu, F. Sun, R. Goei, Y. Zhou, Construction of WO_3–gC_3 Ns_4 composites as efficient photocatalysts for pharmaceutical degradation under visible light, Catalysis Science & Technology, 7 (2017) 2591-2600.
[31] Y. Tu, G. Shao, W. Zhang, J. Chen, Y. Qu, F. Zhang, S. Tian, Z. Zhou, Z. Ren, The degradation of printing and dyeing wastewater by manganese-based catalysts, Science of The Total Environment, 828 (2022) 154390.
[32] G. Vyskočilová, M. Ebersbach, R. Kopecká, L. Prokeš, J. Příhoda, Model study of the leather degradation by oxidation and hydrolysis, Heritage Science, 7 (2019) 1-13.

[33] M. Auffan, M. Pedeutour, J. Rose, A. Masion, F. Ziarelli, D. Borschneck, C. Chaneac, C. Botta, P. Chaurand, J. Labille, Structural degradation at the surface of a TiO_2-based nanomaterial used in cosmetics, Environmental science & technology, 44 (2010) 2689-2694.
[34] D. Pingret, A. Fabiano-Tixier, F. Chemat, Degradation during application of ultrasound in food processing: A review, Food control, 31 (2013) 593-606.
[35] F.M.D. Chequer, D.J. Dorta, D. de Oliveira, Azo dyes and their metabolites: does the discharge of the azo dye into water bodies represent human and ecological risks, Advances in treating textile effluent, 48 (2011) 28-48.
[36] J. Van Dyk, R. Gama, D. Morrison, S. Swart, B. Pletschke, Food processing waste: Problems, current management and prospects for utilisation of the lignocellulose component through enzyme synergistic degradation, Renewable and Sustainable Energy Reviews, 26 (2013) 521-531.
[37] Y. Chen, Y. Wang, Y. Ge, B. Xu, Degradation of endogenous and exogenous genes of Roundup-Ready soybean during food processing, Journal of Agricultural and Food Chemistry, 53 (2005) 10239-10243.
[38] M. Rauf, S.S. Ashraf, Fundamental principles and application of heterogeneous photocatalytic degradation of dyes in solution, Chemical engineering journal, 151 (2009) 10-18.
[39] C.M. Magdalane, K. Kaviyarasu, A. Raja, M. Arularasu, G.T. Mola, A.B. Isaev, N.A. Al-Dhabi, M.V. Arasu, B. Jeyaraj, J. Kennedy, Photocatalytic decomposition effect of erbium doped cerium oxide nanostructures driven by visible light irradiation: investigation of cytotoxicity, antibacterial growth inhibition using catalyst, Journal of Photochemistry and Photobiology B: Biology, 185 (2018) 275-282.
[40] M. Oturan, An ecologically effective water treatment technique using electrochemically generated hydroxyl radicals for in situ destruction of organic pollutants: application to herbicide 2, 4-D, Journal of Applied Electrochemistry, 30 (2000) 475-482.
[41] M. Shang, W. Wang, L. Zhang, H. Xu, Bi_2WO_6 with significantly enhanced photocatalytic activities by nitrogen doping, Materials chemistry and physics, 120 (2010) 155-159.
[42] G. Hu, J. Yang, X. Duan, R. Farnood, C. Yang, J. Yang, W. Liu, Q. Liu, Recent developments and challenges in zeolite-based composite photocatalysts for environmental applications, Chemical Engineering Journal, 417 (2021) 129209.
[43] S. Gélinas, O. Paré-Labrosse, C. Brosseau, S. Albert-Seifried, C.R. McNeill, K.R. Kirov, I.A. Howard, R. Leonelli, R.H. Friend, C. Silva, The binding energy of charge-transfer excitons localized at polymeric semiconductor heterojunctions, The Journal of Physical Chemistry C, 115 (2011) 7114-7119.
[44] Y.P. Zhu, C. Guo, Y. Zheng, S. Qiao, Surface and interface engineering of noble-metal-free electrocatalysts for efficient energy conversion processes, Accounts of Chemical Research, 50 (2017) 915-923.
[45] R. Samal, G. Sanyal, B. Chakraborty, C. Rout, Two-dimensional transition metal phosphorous trichalcogenides (MPX_3): a review on emerging trends, current state and future perspectives, Journal of Materials Chemistry A, 9 (2021) 2560-2591.
[46] N. Mahmood, Y. Yao, J.W. Zhang, L. Pan, X. Zhang, J. Zou, Electrocatalysts for hydrogen evolution in alkaline electrolytes: mechanisms, challenges, and prospective solutions, Advanced Sciences, 5 (2018) 1700464.
[47] L. Cao, Q. Luo, W. Liu, Y. Lin, X. Liu, Y. Cao, W. Zhang, Y. Wu, J. Yang, T. Yao, Identification of single-atom active sites in carbon-based cobalt catalysts during electrocatalytic hydrogen evolution, Nature Catalysis, 2 (2019) 134-141.
[48] H. Yang, M. Driess, P. Menezes, Self-supported electrocatalysts for practical water electrolysis, Advanced Energy Materials, 11 (2021) 2102074.
[49] Y. Surendranath, D. Nocera, Oxygen Evolution Reaction Chemistry of Oxide-Based Electrodes, Progress in Inorganic Chemistry, 57 (2011) 505-560.
[50] L. Gao, X. Cui, C.D. Sewell, J. Li, Z. Lin, Recent advances in activating surface reconstruction for the high-efficiency oxygen evolution reaction, Chemical Society Reviews, 50 (2021) 8428-8469.

[51] G. Janani, Y. Chae, S. Surendran, Y. Sim, W. Park, J.K. Kim, U. Sim, Rational design of spinel oxide nanocomposites with tailored electrochemical oxygen evolution and reduction reactions for zincair batteries, Applied Sciences, 10 (2020) 3165.
[52] Y. Wang, Z. Liang, H. Zheng, R.J. Cao, Recent progress on defect-rich transition metal oxides and their energy-related applications, Chemistry-An Asian Journal, 15 (2020) 3717-3736.
[53] J. Xu, Y. Wang, S.J. Hu, Nanocomposites of graphene and graphene oxides: synthesis, molecular functionalization and application in electrochemical sensors and biosensors. A review, Microchimica Acta, 184 (2017) 1-44.
[54] W. Peng, M. Luo, X. Xu, K. Jiang, M. Peng, D. Chen, T.S. Chan, Y.J. Tan, Spontaneous atomic ruthenium doping in Mo_2CTX MXene defects enhances electrocatalytic activity for the nitrogen reduction reaction, Advanced Energy Materials, 10 (2020) 2001364.
[55] B. Pierozynski, L. Smoczynski, Kinetics of hydrogen evolution reaction at nickel-coated carbon fiber materials in 0.5 M H_2SO_4 and 0.1 M NaOH solutions, Journal of The Electrochemical Society, 156 (2009) B1045.
[56] M. Al-Baghdadi, Modelling of proton exchange membrane fuel cell performance based on semi-empirical equations, Renewable Energy, 30 (2005) 1587-1599.
[57] Z.P. Wu, X.F. Lu, S.Q. Zang, X. Lou, Non-noble-metal-based electrocatalysts toward the oxygen evolution reaction, Advanced Functiona Materials, 30 (2020) 1910274.
[58] L. Bai, L. Gao, B. Conway, Problem of in situ real-area determination in evaluation of performance of rough or porous, gas-evolving electrocatalysts. Part 1.—Basis for distinction between capacitance of the double layer and the pseudocapacitance due to adsorbed H in the H2 evolution reaction at Pt, Journal of Chenical Society, 89 (1993) 235-242.
[59] M.U. Nisa, A.G. Abid, S. Gouadria, T. Munawar, Z. Alrowaili, M. Abdullah, M. Al-Buriahi, F. Iqbal, M.F. Ehsan, M.N. Ashiq, Interfaces, Boosted electron-transfer/separation of $SnO_2/CdSe/Bi_2S_3$ heterostructure for excellent photocatalytic degradation of organic dye pollutants under visible light, Surfaces & Interfaces, 31 (2022) 102012.
[60] M.U. Nisa, S. Manzoor, A.G. Abid, N. Tamam, M. Abdullah, M. Najam-Ul-Haq, M. Al-Buriahi, Z. Alrowaili, Z.M. Mahmoud, M.N. Ashiq, CdSe supported SnO_2 nanocomposite with strongly hydrophilic surface for enhanced overall water splitting, Fuel, 321 (2022) 124086.
[61] M.U. Nisa, S. Gouadria, S. Houda, K. Jabbour, S. Manzoor, S. Aman, M. Najam-Ul-Haq, M.N. Ashiq, Coral like gadolinium doped hematite nanostructure as stable and robust electrocatalyst for oxygen evolution water splitting, Fuel, 338 (2023) 127313.
[62] M. Abudllah, M. Al Huwayz, N. Alwadai, S. Manzoor, M.U. Nisa, P. John, M.I. Ghori, S. Aman, M. Al-Buriahi, M.N. Ashiq, Facile fabrication of ternary CuO/CuS/ZnS for photodegradation of methylene blue, Journal of Korean Ceramics Society, 60 (2023) 569-580.
[63] F. Dionigi, P. Strasser, NiFe-based (oxy) hydroxide catalysts for oxygen evolution reaction in non-acidic electrolytes, Advanced Energy Materials, 6 (2016) 1600621.
[64] C. Jiao, X. Bo, M.J. Zhou, Electrocatalytic water splitting at nitrogen-doped carbon layers-encapsulated nickel cobalt selenide, Journal of Energy Chemistry, 34 (2019) 161-170.
[65] Z. Fang, L. Peng, H. Lv, Y. Zhu, C. Yan, S. Wang, P. Kalyani, X. Wu, G. Yu, Metallic transition metal selenide holey nanosheets for efficient oxygen evolution electrocatalysis, ACS Nano, 11 (2017) 9550-9557.
[66] C. Sun, X. Guo, J. Zhang, G. Han, D. Gao, X. Gao, Rechargeable Zn-air batteries initiated by nickel–cobalt bimetallic selenide, Journal of Energy Chemistry, 38 (2019) 34-40.
[67] J. Chen, J. Chen, H. Cui, C. Wang, Electronic Structure and Crystalline Phase Dual Modulation via Anion–Cation Co-doping for Boosting Oxygen Evolution with Long-Term Stability Under Large Current Density, ACS Applied Materials Interfaces, 11 (2019) 34819-34826.

[68] C. Xu, Q. Li, J. Shen, Z. Yuan, J. Ning, Y. Zhong, Z. Zhang, Y. Hu, A facile sequential ion exchange strategy to synthesize $CoSe_2/FeSe_2$ double-shelled hollow nanocuboids for the highly active and stable oxygen evolution reaction, Nanoscale, 11 (2019) 10738-10745.
[69] J. Wan, W. Ye, R. Gao, X. Fang, Z. Guo, Y. Lu, D. Yan, Synthesis from a layered double hydroxide precursor for a highly efficient oxygen evolution reaction, Inorganic Chemistry Frontiers, 6 (2019) 1793-1798.
[70] G. Wang, H. Wang, T. Chen, Y. Tan, Ni_{1-x} Ms_x Se_2 (M= Fe, Co, Cu) nanowires as anodes for ammonia-borane electrooxidation and the derived Ni_{1-x} M_x Se_{2-y}–OOH ultrathin nanosheets as efficient electrocatalysts for oxygen evolution, Journal of Materials Chemistry A, 7 (2019) 16372-16386.
[71] J. Cao, K. Wang, J. Chen, C. Lei, B. Yang, Z. Li, L. Lei, Y. Hou, K. Ostrikov, Nitrogen-doped carbon-encased bimetallic selenide for high-performance water electrolysis, Nano-Micro Letters, 11 (2019) 1-11.
[72] A.A. Mirghni, K.O. Oyedotun, O. Olaniyan, B.A. Mahmoud, N.F. Sylla, N. Manyala, Electrochemical analysis of Na–Ni bimetallic phosphate electrodes for supercapacitor applications, RSC advances, 9 (2019) 25012-25021.
[73] F. Zhang, Y. Pei, Y. Ge, H. Chu, S. Craig, P. Dong, J. Cao, P.M. Ajayan, M. Ye, J. Shen, Controlled synthesis of eutectic $NiSe/Ni_3Se_2$ self-supported on Ni foam: An excellent bifunctional electrocatalyst for overall water splitting, Advanced Materials Interfcaes, 5 (2018) 1701507.
[74] L. Wang, B. Zhu, J. Zhang, J.B. Ghasemi, M. Mousavi, J. Yu, S-scheme heterojunction photocatalysts for CO2 reduction, Matter, 5 (2022) 4187-4211.
[75] L. Zhang, J. Zhang, H. Yu, J. Yu, Emerging S-scheme photocatalyst, Advanced Materials, 34 (2022) 2107668.
[76] Q. Xu, S. Wageh, A.A. Al-Ghamdi, X. Li, Design principle of S-scheme heterojunction photocatalyst, Journals of Materials Science & Technology, 124 (2022) 171-173.

Declaration Statement

The authors declare that they have no known competing financial interests or personal relationships that could have appeared to influence the work reported in this paper.

The manuscript has not been published previously, and is not under consideration for publication elsewhere. It is also stated that the work is original. The publication is approved by all authors and tacitly or explicitly by the responsible authorities where the work was carried out. If accepted, it will not be published elsewhere in the same form, in English or in any other language, including electronically without the written consent of the copyright-holder. In addition, the authors have no conflicts of interest to declare.